Can a sheet-like low-velocity region form an elongated Large Igneous Province?

Atsuko Namiki

Department of Earth and Planetary Science, University of Tokyo, 7-3-1, Hongo, Bunkyo, Tokyo 113-0033, Japan (namiki@eps.s.u-tokyo.ac.jp)

Kenta Sueyoshi and Nozomu Takeuchi

Earthquake Research Institute, University of Tokyo, Yayoi 1-1-1, Bunkyo, Tokyo 113-0032, Japan

[1] High-resolution tomography of the lower mantle has revealed the existence of another chemically distinct region with low-velocity and a sheet-like structure beneath the western Pacific. On the other hand, Large Igneous Provinces (LIPs) sometimes have elongated shapes. If a sheet-like upwelling reaches the Earth's surface while maintaining its shape, an elongated LIP may form. In order to test this hypothesis, we perform a series of experiments and investigate the stability of a buoyant sheet. The experimental results show that the buoyant fluid accumulates at the top of the sheet to form a buoyant cylinder. The gravitational instability divides the cylinder into several plume heads. We develop a model to explain the growth of the buoyant cylinder and the time scale until instability begins. Our model shows that a thin sheet-like upwelling with a width of 200 km, a small density difference from the ambient mantle, 10 kg m^{-3}, and a high supply rate of buoyant fluid, 0.1 m yr^{-1}, can reach the Earth's surface while maintaining its shape. We thus infer that LIPs with an elongated shape can be generated by sheet-like upwellings. The width of the observed sheet-like low-velocity region beneath the western Pacific is 500 km and is marginally sufficient to form an elongated LIP.

1. Introduction

[2] Seismological observations have revealed Large Low-Shear-Velocity Provinces (LLSVPs) in the deep mantle, likely representing chemically distinct materials [e.g., *Garnero and McNamara*, 2008]. The LLSVP beneath southern Africa elongates from north to south about 8000 km and is about 3500 km across [*Ni and Helmberger*, 2003; *Wang and Wen*, 2007]. This region may be thermally buoyant and chemically dense. Although chemical piles are usually described as dome-like structures, part of the LLSVP beneath the southern Africa is frequently described as ridge-like because of its elongated shape.

[3] *Takeuchi* [2012] provides a high-resolution image of whole-mantle SH velocity structures by waveform tomography and finds another low-velocity region beneath the western Pacific, which also has an elongated ridge-like structure. Figures 1a and 1b show the SH velocity structures in a horizontal cross section at a depth of 2100 km and in a vertical cross section, respectively. The low-velocity region is denoted by a reddish color. The elevation of the low-velocity region reaches 700 km with a width of 800 km and a length of 2000 km. These dimensions are consistent with those measured by *He and Wen* [2009].

[4] Above this ridge-like structure, a thin (500 km) sheet-like low-velocity region extends (marked by

a green rectangle in Figures 1b and 6 in *Takeuchi* [2012]). A narrow plume above a dome-like chemical pile is expected on the basis of thermochemical convection experiments [e.g., *Davaille*, 1999], and has been observed [*Sun et al.*, 2010]. If a pile has a two-dimensional ridge-like structure rather than a three-dimensional dome, an upwelling above it may have a two-dimensional sheet-like structure rather than a pipe-like plume. We thus infer that a sheet-like upwelling can exist above a ridge-like structure as shown by schematic diagrams in Figure 1. Here we call this structure the Sheet-like-Low-Velocity Region in the Pacific (SLVRP).

[5] If this SLVRP is chemically distinct from the ambient mantle, a sharp boundary separates the
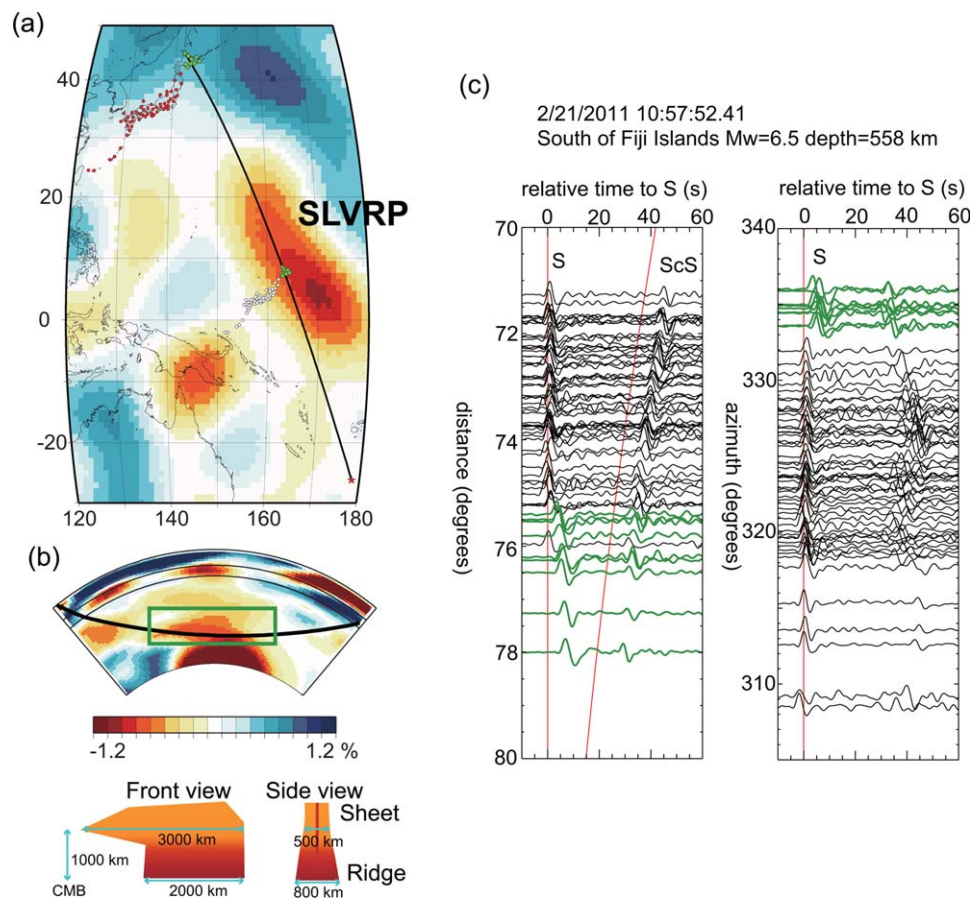

Figure 1. Shear wave anomaly map of SH18CEX model obtained from waveform inversion [*Takeuchi*, 2012]. (a) Horizontal cross section at a depth of 2100 km. Green and red dots in Japan show the loci of stations, and green and white dots in the Pacific are the respective bottoming points of the rays. (b) Vertical cross section at the locations indicated by the black curve in Figure 1a. Schematic diagrams show approximate dimensions of shear wave anomaly. (c) Transverse component of waveforms for the event (Mw 6.5) on 21 February 2011 south of the Fiji Islands (red star in Figure 1a) recorded in Japan by F-net aligned with respect to the S arrival time predicted for PREM. The left and right parts in Figure 1c show the distance and azimuth dependence, respectively. Waveforms are filtered between 3.3 and 100 s. The black curves in Figures 1a and 1b are an example of ray paths. The waveforms shown by green and black curves are bottoming and observed at the points denoted by green and white/red dots in Figure 1a, respectively. Only green curves traveling through the SLVRP show a clear delay of arrivals.

SLVRP from the ambient mantle similar to LLSVPs [e.g., *Ni et al.*, 2002; *To et al.*, 2005]. Figure 1c shows the waveforms of an event south of the Fiji Islands recorded in Japan. Only the green curves traveling through the SLVRP show a clear delay (about 5 s) of the *S* wave arrival. The bottoming depths of the ray paths for the *S* waves are between 2100 and 2200 km. We thus infer that the SLVRP is also chemically distinct from other parts of the mantle at least to a height of 700 km.

[6] The mechanisms underlying the formation of a locally elevated shape of LLSVPs have been investigated extensively as a problem of thermochemical convection [*Olson and Kincaid*, 1991; *Davaille*, 1999; *Gonnermann et al.*, 2002; *Namiki*, 2003; *McNamara and Zhong*, 2005; *Tan and Gurnis*, 2007; *Jaupart et al.*, 2007; *Deschamps et al.*, 2011; *Tackley*, 2012]. Since LLSVPs are regarded as chemically distinct regions, they may have a positive density anomaly by the chemical effect and a negative density anomaly by the thermal effect. When the thermal effect overwhelms the chemical effect, some parts of LLSVPs can ascend [e.g., *Olson and Kincaid*, 1991; *Davaille*, 1999; *Tan and Gurnis*, 2007].

[7] The manner in which a buoyant fluid ascends has also been extensively investigated. A buoyant fluid often ascends as plumes that are spherical heads accompanied by tails [e.g., *Whitehead and Luther*, 1975; *Griffiths and Campbell*, 1990; *Bercovici and Kelly*, 1997; *Kumagai et al.*, 2008]. A few studies have shown that an initially sheet-like upwelling forms a buoyant cylinder at the top of the sheet [*Kerr and Lister*, 1988]. The cylinder eventually separates into several spherical heads [*Olson and Singer*, 1985; *Lister and Kerr*, 1989; *Kerr et al.*, 2008; *Lister et al.*, 2011]. It is not obvious, however, how high the buoyant sheet can reach before it separates into spherical heads.

[8] On the other hand, voluminous magma emplacements, known as Large Igneous Provinces (LIPs), have been observed on the Earth's surface. Although substantial debates about their origin continue, collisions of plume heads with the lithosphere likely generate LIPs [e.g., *Griffiths and Campbell*, 1990; *Coffin and Eldholm*, 1994; *Ernst et al.*, 2005]. The sources of LIPs are considered to be different from the typical pyrolitic mantle and may include the eclogite component [*Cordery et al.*, 1997]. LIPs may originate from the deeper part of the mantle and entrain some portions of chemically separated reservoirs [*van Keken et al.*, 2002]. Indeed, the spatial distribution of LIPs correlates with LLSVP margins [*Torsvik et al.*, 2006; *Tan et al.*, 2011; *Steinberger and Torsvik*, 2012].

[9] Reconstructed LIPs sometimes show elongated shapes in specific directions [*Elliot et al.*, 1999; *Taylor*, 2006; *Bryan and Ernst*, 2008]. For example, the Ferrar LIP, which was emplaced at ~180 Ma, extended more than 3000 km within a narrow width [*Elliot et al.*, 1999]. If a spherical plume head forms a LIP, it is more likely to become round or a triple junction. However, if the observed SLVRP, which has a sheet-like shape, ascends continuously and collides with the lithosphere, an elongated or ridge-like LIP may form.

[10] We infer that the observed sheet-like shape of the SLVRP originates from the particular pattern of mantle convection as is discussed in *Takeuchi* [2012]. At the Rayleigh number of the mantle convection, the convection pattern usually consists of ascending plumes with spherical heads and sheet-like downwellings [e.g., *Bercovici et al.*, 1989]. In mantle convection, however, there are many causes of the elongation of convection cells laterally and of two-dimensional sheet-like upwellings. The plate-like behavior of mantle convection arises from the plastic yielding combined with strongly temperature-dependent viscosity [e.g., *van Heck and Tackley*, 2008; *Nakagawa et al.*, 2009]. The subducted slab pushes the chemically distinct region and forms a ridge-like structure of the LLSVPs [*McNamara and Zhong*, 2005]. Sheet-like upwellings form at the edge of the chemical pile [*Steinberger and Torsvik*, 2012]. We thus infer that the sheet-like shape of an upwelling is plausible in the mantle convection as an initial condition of ascending.

[11] Accordingly, we here assume that there exists a buoyant sheet similar to the SLVRP made by the mantle convection as an initial condition. We conduct experiments using this initial condition. Based on our experiments, we estimate the conditions in which such a sheet-like upwelling can reach the Earth's surface before the gravitational instability separates it into several spherical plume heads. If a sheet-like upwelling satisfies this condition, it can form an elongated LIP.

2. Experimental Methods

[12] In order to simulate the shape evolution of a buoyant sheet, we conduct a series of experiments with a tank, shown in Figure 2, with inner dimensions of 0.35 m width, 0.25 m depth, and 0.46 m
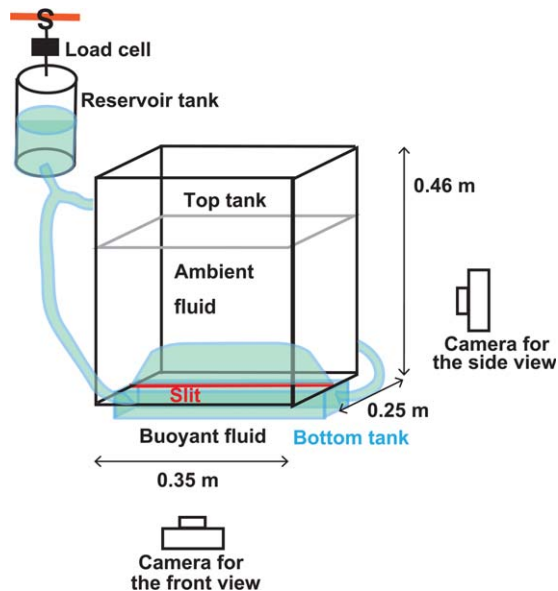
Figure 2. A schematic diagram of the experimental apparatus.

height, featuring a slit at the bottom with a 2 mm width. Buoyant fluid is injected through the slit from a reservoir tank. The edge of the slit is polished so as not to cause disturbances. Prior to the beginning of the experiments, the slit is covered by a thin plate (gate) to prevent the injection of buoyant fluids. We start experiments by sliding the gate horizontally so as not to affect the ascending manner of the buoyant fluid. The reservoir tank is located higher than the surface of the ambient fluid so that an upwelling sheet forms. The reservoir tank is weighed by a load cell to calculate the fluid flux q. The measured fluid flux is constant during an experiment. The flux of buoyant fluid is varied by changing the height of the reservoir tank (0.4–1.2 m).

[13] We use syrup solutions as analogues for mantle materials. The ambient and buoyant fluids are miscible. The density ρ and viscosity μ of the syrup are varied by changing the water content and adding salt. Since the viscosity of the mantle materials depends on temperature and the viscosity inside the upwellings is lower than that of the surrounding mantle, we use a less viscous buoyant fluid. The parameters in which the experiments are conducted are summarized in Table 1.

[14] Front and side views of the experiments are recorded by two digital video cameras with resolutions of 1920 × 1080 at 30 frames/s. The time evolutions of the height and shape of the buoyant fluid are analyzed using MATLAB. Image analysis is conducted for the front view.

[15] In order to apply the phenomena observed in our experimental results to the Earth's mantle, the calculated Reynolds number, Re, should be Re ≪ 1. In our experiments, the maximum plume head velocity is less than 0.01 m s^{-1}, and the possible maximum plume radius is 0.15 m, thus, Re ≪ 1.

[16] In the thermochemically convecting mantle, the upwelling region is formed by the thermal buoyancy and is chemically heavier than the surrounding mantle. On the other hand, in our experiments, we use chemically buoyant fluid to form a buoyant sheet. A thermochemical plume sometimes cools as it ascends, loses thermal buoyancy, and then shows complex behaviors [e.g., *Farnetani and Samuel*, 2005; *Lin and van Keken*, 2006; *Kumagai et al.*, 2008]. For simplification, we conduct our experiments with a chemically buoyant fluid that does not lose buoyancy during its ascent. Our simple experiments help us to make an

Table 1. List of Experiments and Their Parameters[a]

μ_a (Pa s)	μ_i (Pa s)	ρ_a (kg/m^3)	ρ_i (kg/m^3)	q (× 10^{-6}) (m^2/s)	Measured t_i (s)	Height at t_i (m)	Equation (7) (s)	Equation (8) (s)	Equation (10) (s)	
10	0.5	1415	1342	13.7	45	0.065	19	2	4	
10	0.6	1415	1342	10.8	31	0.055	19	3	5	
10	0.4	1415	1342	9.7	38	0.056	18	3	5	
10	0.3	1415	1342	1.3	39	0.025	16	7	9	
16	2.3	1414	1380	4.1	72	0.039	83	10	17	
16	2.3	1414	1380	2.2	243	0.098	83	14	21	
16	2.3	1414	1380	1.9	175	0.065	83	15	23	Figure 3
16	2.3	1414	1380	1.2	186	0.081	83	19	26	
16	2.3	1414	1380	0.8	203	0.039	83	24	30	
78	2.2	1430	1340	2.6	293	0.096	102	12	23	
78	2.2	1430	1340	1.1	518	0.089	102	18	31	

[a]μ: viscosity, ρ: density, and q: flux of the buoyant fluid per unit length. Subscripts a and i indicate ambient and buoyant fluids, respectively. t_i is the measured time scale until undulations develop at the top of a buoyant sheet after an experiment begins. The measured height at t_i and time scales estimated by equations (7), (8), and (10) are also listed. See text for details. The corresponding figure number in which the experimental result is shown is denoted.

Geochemistry
Geophysics
Geosystems

G^3

NAMIKI ET AL.: A SHEET-LIKE UPWELLING

10.1002/ggge.20182

3. Experimental Results

[17] Figure 3a and Animation 1 (supporting information)[1] show the time evolution of the buoyant fluid. At 0 s, the buoyant fluid is located between the slit at the bottom of the tank, observed as the blue line in the side view. At 80 s, the front view shows that the buoyant fluid has a sheet-like shape. The side view, however, shows that the top of the buoyant sheet is wider than that of the slit (2 mm), indicating that the buoyant fluid is accumulating at the top of the sheet. There exist some nodes at the top of the buoyant sheet, suggesting that instability is occurring. At 160 s, a darker-blue region appears at the top of the buoyant sheet from the front view, as shown by the red rectangle, which is round from the side view, suggesting that the accumulating buoyant fluid at the top of the sheet has a cylindrical shape. However, the side view also shows that the radius of the cylinder is not unique, as shown by the red and pink arrows. We thus interpret the snapshots at 160 s to mean that some plume heads are developing in the cylindrical fluid. There are fewer nodes at 160 s than at 80 s. At 240 s, the cylindrical region separates into several spherical heads even in the front view. The heads ascend with tails faster than the sheet (400 s).

[18] Other experiments show similar characteristics. Buoyant fluid accumulates into a cylinder and separates into several plume heads. In experiments with a less-viscous ambient fluid, instability begins sooner. In a comparison of experiments using the same ambient fluid, a faster fluid supply makes the plume heads larger.

4. Model

4.1. Time Evolution of the Shape of the Buoyant Fluid

[19] In our experiments, we find that the buoyant fluid ascending from a line source forms a sheet-like upwelling and then accumulates at the top of the upwelling sheet into a cylindrical shape. We here develop a model to explain the growth rate of the fluid cylinder. We assume that the growth of the fluid cylinder is determined by the upwelling velocity of the cylinder, U, and the flux of the

---

[1]Additional supporting information may be found in the online version of this article.

buoyant fluid, q. When the cylinder ascends, the fluid sheet that connects the source and the cylinder elongates. Some part of the buoyant fluid supplied from the source is consumed to build the newly created sheet. The remainder of the fluid supply flows into the cylinder and increases its radius. This phenomenon is described as follows

$$2\pi r \frac{dr}{dt} = q - Uw, \tag{1}$$

where r is the radius of the fluid cylinder, t is the elapsed time after the fluid supply begins, q is the flux of the buoyant fluid per unit length, and w is the width of the fluid sheet. Visual observations indicate that the width of the sheet does not change significantly during the ascent. We thus use the initial width of $w \sim 2 \times 10^{-3}$ m for the ascending sheet.

[20] It is reasonable to consider that the ascending velocity of the buoyant cylinder is scaled as

$$U = \frac{C\Delta\rho g r^2}{\mu_a}, \tag{2}$$

where $\Delta\rho = \rho_a - \rho_i$ is the density difference between the ambient ρ_a and buoyant ρ_i fluids, $g = 9.8$ m s^{-2} is the gravitational acceleration, μ_a is the viscosity of the ambient fluid, and C is a constant.

[21] We solve equations (1) and (2) with the initial condition $r = w/2$ for $t = 0$ and obtain

$$r = \sqrt{\frac{q\mu_a}{C\Delta\rho gw}\left\{1 - \left(1 - \frac{C\Delta\rho gw^3}{4q\mu_a}\right)e^{-\frac{C\Delta\rho gw}{\pi\mu_a}t}\right\}}. \tag{3}$$

[22] This equation indicates that the cylinder radius asymptotically approaches

$$r_a = \sqrt{\frac{q\mu_a}{C\Delta\rho gw}}. \tag{4}$$

[23] In equation (3), the term inside the parentheses should be positive; otherwise, the radius of the cylinder decreases as time elapses. The required condition is written as

$$\frac{q}{w} > \frac{C\Delta\rho gw^2}{4\mu_a}. \tag{5}$$

[24] When a condition does not meet equation (5), it means that a buoyant cylinder with a radius $w/2$ ascends faster than the supply of the buoyant fluid.
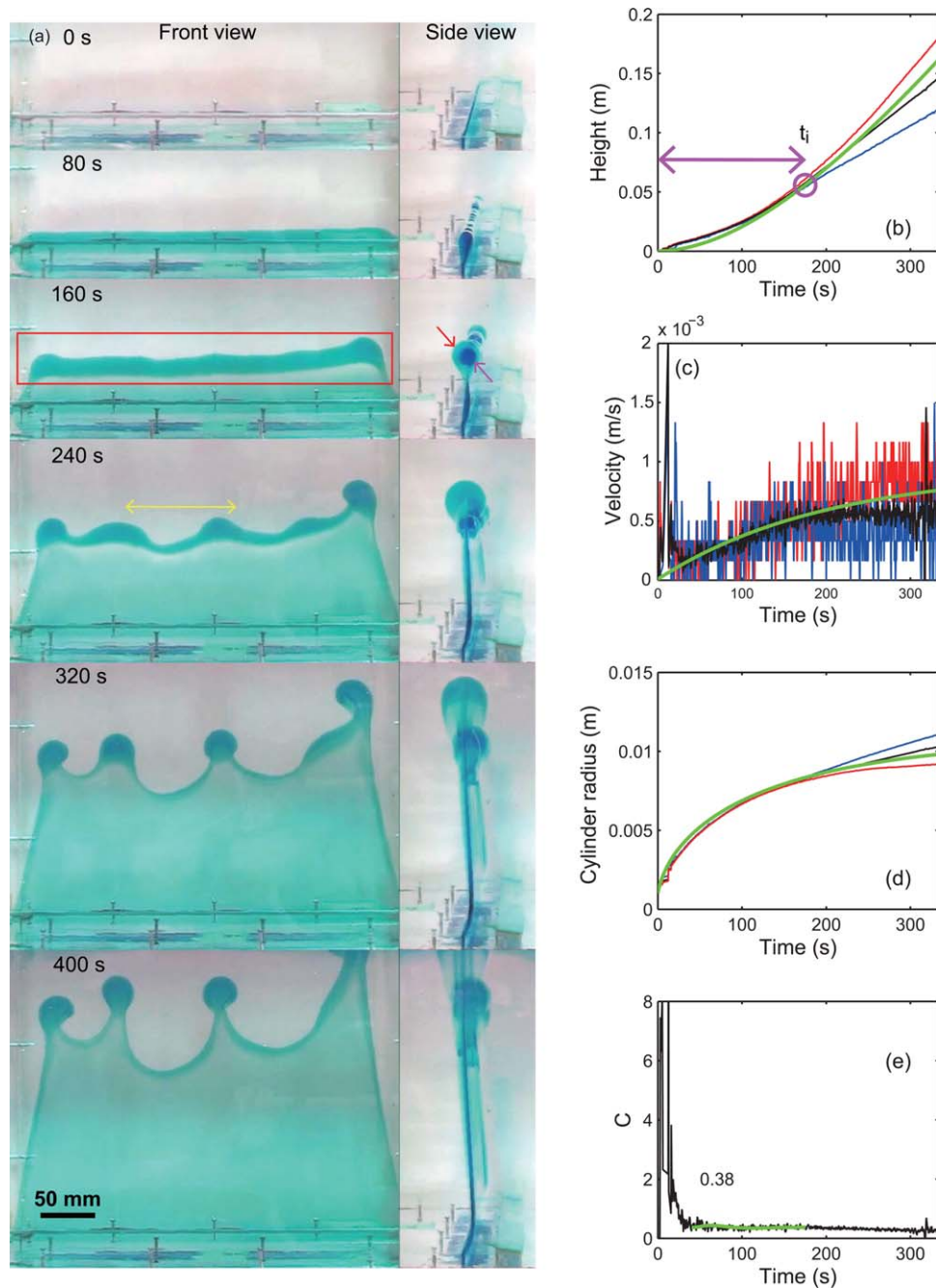
Figure 3. (a) Images of the time evolution of the buoyant fluid. The blue region indicates the buoyant fluid. The numbers indicate the time elapsed after the ascent begins. The left hand and right hand figures show front and side views, respectively. The yellow arrow indicates the spatial range in which the time scale of instability t_i is measured. Animation of this figure is provided as Animation 1. (b) Measured and calculated heights of the buoyant fluid as a function of time. Red, blue, and black curves are measured heights and show the maximum, minimum, and averaged heights within the spatial range denoted by the yellow arrow, respectively. The green curve shows the calculated height by the time integration of equation (2) with equation (3). We use the same colors for the curves in Figure 3c and 3d. The purple circle and the arrow indicate the measured time scale t_i until instability is observed after the experiment begins. (c) Measured and calculated velocities for the ascending buoyant fluid. The green curve is calculated by equation (2). (d) Estimated cylinder radius of the buoyant fluid from the observation and our model denoted in equation (3). (e) The estimated prefactor C in equation (2) by the averaged ascending velocity of the buoyant fluid in Figure 3c. In Figures 3b–3d, we use $C = 0.38$ estimated in Figure 3e.

[25] This model includes an unknown prefactor C. In order to estimate C, we here calculate the ascending velocity of the buoyant cylinder from the experiment and compare it with our model. The red, blue, and black curves in Figure 3b show the maximum, minimum, and averaged heights of the buoyant fluid, respectively, within the spatial range denoted by the yellow arrow in Figure 3a. We calculate the ascending velocity of the buoyant fluid as shown in Figure 3c from the time derivative of heights. Since we know the flux of buoyant fluid q and ascending velocity U, we can calculate the cylinder radius for each time step by using equation (1) with the initial condition $r = w/2$. The estimated cylinder radius is denoted in Figure 3d. We now know both the ascending velocity U and the cylinder radius r, and can calculate the prefactor C in equation (2). The black curve in Figure 3e shows that the estimated C converges to an asymptotic value around 0.4.

[26] Since the prefactor C should be calculated for the duration in which the buoyant fluid maintains a cylindrical shape, and since there may be initial perturbations in experiments, we calculate the mean value for the time duration denoted by a green line in Figure 3e and obtain 0.38. We estimate the prefactor C for other experiments with the same method denoted by the black curve in Figure 3e and obtain similar characteristics and values. In other experiments, however, the buoyant fluid remains cylindrical for only short periods of time, and it is difficult to define the time duration for averaging. We thus use $C = 0.38$ as a representative value for the cylinder-shaped fluid with nodes. This value is close to that for a viscosity-free sphere, 1/3.

[27] We calculate the cylinder radius, ascending velocity, and height of the buoyant fluid by using equations (2) and (3), as denoted by the green curves in Figures 3b–3d. Since our model does not include the phenomena after instability grows, we can compare the green curves with the measurements only until instability begins, which is recognizable by increasing differences between the red and blue curves. Except for the very beginning of the experiments (<20 s), the model shows good agreement with the measurements until instability begins. At the beginning of the experiments, the flux of the buoyant fluid suddenly changes which may cause unexpected perturbations. In addition, at very low heights, it is difficult to measure the height of the buoyant fluid accurately. We thus conclude that our model reasonably explains the experimental results.

4.2. Time Scale Until Instability Begins

[28] We here consider the time scale t_i that elapses before the fluid sheet turns into separated plume heads after the sheet begins to ascend. We first consider the time scale observed in our experiments.

[29] When gravitational instability occurs, the local variation in the height of the buoyant fluid should increase. After instability fully develops, the velocity of the plume head is not likely accelerated significantly. If the size of the plume head is fixed, the ascending velocity becomes constant. We thus calculate the time at which the time derivative of the height variation in the logarithmic scale, $d\log(h_{max} - h_{min})/dt$, becomes its maximum, where h_{max} and h_{min} are red and blue curves in Figure 3b, respectively. In other experiments, we chose the loci to calculate $h_{max} - h_{min}$ as follows. Its length scale includes $1 \sim 2$ undulations at the top of the sheet. The loci exclude the edge of the cylinder and regions disturbed by bubbles. We plot the calculated time with a purple circle in Figure 3b and find that it explains the time when the fluid sheet has undulations, that is, when the instability grows. We thus use the time duration denoted by the purple arrow in Figure 3b, until the time denoted by the purple circle after the experiment starts, as the time scale for the instability to begin t_i. The measured time scale t_i is summarized in Table 1.

[30] Next, we consider two models for the time scales until the gravitational instability begins. Using linear stability analysis, *Lister and Kerr* [1989] formulate the required time scale τ for instability to grow in a buoyant cylinder with a constant radius of a,

$$\tau = C_g \frac{\mu_a}{\Delta \rho g a}. \tag{6}$$

[31] The prefactor C_g in the above equation is described in Appendix A. The important characteristic of equation (6) is that the time scale for the growth of instability depends inversely on the radius of the buoyant cylinder.

[32] In our experiments, the cylinder radius r increases as time elapses so that the time scale τ becomes shorter. The cylinder radius r grows from half the width of the fluid sheet $w/2$ to the asymptotic radius written in equation (4). Substituting these two radii into equation (6), we can estimate the longest τ_1 and shortest τ_s time scales to grow instabilities

$$\tau_1 = C_g \frac{\mu_a}{\Delta \rho g w} \quad (7)$$

$$\tau_s = C_g \sqrt{\frac{C \mu_a w}{\Delta \rho g q}}. \quad (8)$$

[33] In Table 1, we compare these time scales with the measured time scale until the gravitational instability begins t_i. The estimated time scales in equations (7) and (8) are shorter than the measured time scale t_i. We thus infer that the time scale until instability begins t_i depends on the time scale for the growth of the cylinder rather than that for the growth of instability.

[34] In equation (3), the time scale until the cylinder radius r approaches the asymptotic value is described as

$$t_1 = \frac{\pi \mu_a}{C \Delta \rho g w}. \quad (9)$$

[35] We plot t_1 by circles in Figure 4 as a function of the measured time scale t_i, showing good correlation. In the experiment denoted by the open blue circle, bubbles are observed in considerable numbers, unlike the case in other experiments. We infer from this that bubbles excite perturbations and cause instabilities on a shorter time scale.

[36] Another possible time scale t_2 may be the time when the growth rate of the instability r/τ becomes faster than that of the cylinder radius

Figure 4. Comparison between the measured t_i and estimated time scales t_1 and t_2 until instability occurs. Circles and crosses indicate t_1 and t_2, respectively. See text for details. The marker colors (red, blue, and green) show the difference in the ambient fluid used in the experiments in the order shown in Table 1. In the experiment denoted by an open blue circle, a substantial amount of bubbles is observed. They may affect the time scale until instability begins.

dr/dt. In other words, if the height difference induced by gravitational instability grows faster than the change in the cylinder radius, that undulation continues to grow. We here calculate dr/dt and τ using equations (1) and (6), respectively. Here τ is the time scale required to grow the instability for a buoyant cylinder with a constant radius a. In our experiments, the cylinder radius r is time dependent. We thus calculate radius r using equation (3) and substitute it for a in equation (6). Prefactors C_g in equation (6) are calculated according to *Lister et al.* [2011] as written in Appendix A. We then calculate the time t_2 where $dr/dt = r/\tau$ and plot it as a cross in Figure 4. Figure 4 shows that t_1 and t_2 indicate similar trends, but t_2 is systematically shorter than the measured t_i.

[37] If we can neglect the newly created sheet Uw in equation (1), the time scale t_2 can be written in a simple analytical form. Neglecting Uw, the growth rate of the cylinder radius becomes $dr/dt = q/2\pi r$. Integration of this equation generates time-dependent cylinder radius $r = \sqrt{qt/\pi}$. The time derivative of r generates the growth rate of the cylinder radius $dr/dt = \sqrt{q/\pi t}/2$. Again, comparing dr/dt and r/τ, we can calculate the analytical form of t_{2a} for the case with small Uw.

$$t_{2a} = \left(\frac{\pi C_g^2 \mu_a^2}{4 \Delta \rho^2 g^2 q} \right)^{1/3}. \quad (10)$$

[38] We calculate t_{2a} and denote them in Table 1. The calculated t_{2a} shows similar time scales of those plotted in Figure 4 and shorter than the measured time scales t_i.

[39] In Figure 4, t_1 and t_2 show similar trends, and *Lister et al.* [2011] report that the observed time scale of the instability is 5 times τ. Figure 4 suggests that a product of a constant factor and t_2 can explain the observed t_i. However, the observed t_i in our experiments is longer than $5t_2$.

[40] We observed a reduction in the number of nodes during 80–160 s in the side view of Figure 3a. This reduction in nodes suggests that the most unstable wavelength can change even after instability begins to grow. It is well known that the most unstable wavelength is scaled with the cylinder radius [*Kerr and Lister*, 1988]. We thus infer that, even when the instability is halfway to growing, the number of nodes can decrease according to the increase in the cylinder radius. We thus consider that the time scale until the cylinder radius
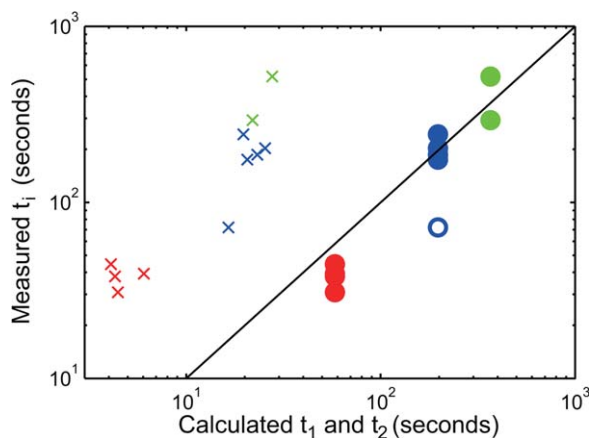
reaches the asymptotic value t_1 explains the time scale t_i after which gravitational instability is observed. Here there is a limitation on the parameter range in our experiments. Experiments with wider ranges of parameters will help distinguish the difference between t_1 and t_2.

5. Discussion

[41] In this section, we apply our model describing the evolution of sheet-like upwellings to the Earth's mantle.

5.1. A Regime for the Growth of a Buoyant Cylinder

[42] In order to apply our model described in equations (1)–(3) to the Earth's mantle, the conditions surrounding the sheet-like structure should satisfy equation (5). In Figure 5, we estimate the parameter range that satisfies equation (5).

[43] Here the density inside the sheet is less than that for the ambient mantle. Thus, the larger density difference $\Delta\rho$ indicates a more buoyant force. We assume the following other parameters: the viscosity of the ambient mantle is 10^{21} to 10^{23} Pa·s [*Mitrovica and Forte*, 2004], gravitational acceleration is $g = 9.8$ m s^{-2}, and the prefactor $C = 0.38$ in equation (2) is the same as that for our experiments. Since there are no quantitative measurements of the rate at which the buoyant fluid in the mantle is supplied, we assume that the supply rate is on the same order of magnitude as the subduction velocity of slabs, $0.01 - 0.1$ m yr^{-1}. This is because the supply of buoyant fluid should be a part of the mantle convection. The subduction velocity of slabs is a typical velocity of the mantle convection. In another aspect, subducting slabs may push a hot thermal boundary to supply buoyant fluid into the sheet-like structure [*Steinberger and Torsvik*, 2012].

[44] The important feature of Figure 5 is that a buoyant sheet having a thinner width and a smaller density difference from the ambient mantle can satisfy equation (5). Here the horizontal green bar indicates the observed width of the SLVRP, 500 km. The pink region indicates the possible density difference attributable to thermal expansion, in which we assume the temperature difference between the inside and outside of a sheet as $\Delta T > 500$ and $> 1000°C$, the thermal expansion as $\alpha = 10^{-5}$ K^{-1} [*Oganov et al.*, 2001], and the density of the mantle rock as $\rho = 5000$ kg m^{-3}.
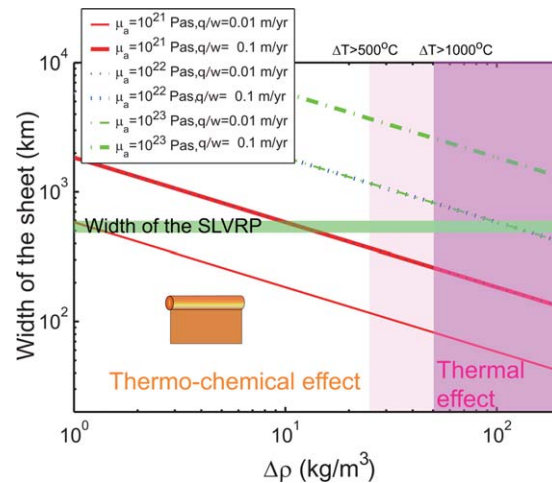

Figure 5. Each line shows the maximum width of a sheet satisfying equation (5). Red solid, blue dotted, and green dashed-dotted lines indicate that the viscosities of the ambient mantle are 10^{21}, 10^{22}, and 10^{23} Pa·s, respectively. Thinner and thicker lines indicate that the areal supply rates of buoyant fluids q/w are 0.01 and 0.1 m yr^{-1}, respectively. The green horizontal bar indicates 500 km and corresponds to the observed width of the SLVRP. Pink regions indicate the possible density differences attributed to thermal expansions for temperature differences between the inside and outside of the buoyant sheet of $\Delta T > 500°C$ and $\Delta T > 1000°C$, thermal expansion of $\alpha = 10^{-5}$ K^{-1} [*Oganov et al.*, 2001], and density of the mantle rock of $\rho = 5000$ kg m^{-3}.

[45] When the density difference between the inside and outside of the buoyant sheet is less than < 10 kg m^{-3}, most of the lines, except for the thin red line, exceeds the horizontal green bar. If the sheet-like structure is compositionally the same as the surrounding mantle, a temperature anomaly of $> 500°C$ generates a density difference > 25 kg m^{-3}. Our model is not applicable to the SLVRP for a low-viscosity mantle $\mu_a \leq 10^{21}$ Pa·s and a low supply rate of buoyant fluid. A seismological observation [*Takeuchi*, 2012] suggested that the SLVRP is chemically distinct from the surrounding mantle. If the SLVRP is chemically denser than the surrounding mantle such that the total density difference from the surrounding mantle is lower than that estimated solely by the thermal effect, we can apply our experimental results to the SLVRP in a wider range of parameters.

[46] If the viscosity of the surrounding mantle is large enough $> 10^{23}$ Pa·s, even with a larger density difference between inside and outside the sheet-like structure > 25 kg m^{-3}, we can apply our experimental results to the SLVRP.

5.2. Possible Conditions for the Formation of an Elongated LIP

[47] We here consider the time evolution of a buoyant sheet in the Earth's mantle. We use the conditions satisfying equation (5) estimated in Figure 5. Figure 6a shows the time evolution of sheet heights with variable conditions. The estimated timings of instabilities t_1 are also denoted by crosses. We can find crosses on most curves, suggesting that most buoyant sheets do not reach the surface of the Earth (3000 km) before gravitational instability separates the buoyant cylinder into several plume heads. Only in the case denoted by the thick blue solid curve, the buoyant sheet can reach the surface of the Earth before t_1. In this case, we adopt the following conditions: the width of the sheet is $w = 200$ km, the density difference is

$\Delta\rho = 10$ kg m^{-3}, and the areal supply rate of the buoyant fluid is $q/w = 0.1$ m yr^{-1}.

[48] Since the time scale until gravitational instability occurs, denoted in equation (9), inversely depends on w and $\Delta\rho$, a thinner sheet with a smaller density difference can maintain its shape longer. On the other hand, the time evolution of the sheet height obtained by the integration of equation (2) with equation (3) is written as

$$h = \frac{q}{w}t + \left(\frac{q}{w}t_1 - \frac{\pi w}{4}\right)\left(e^{-t/t_1} - 1\right). \qquad (11)$$

[49] For a large t, equation (11) approaches asymptotically to $h = qt/w$. Accordingly, a higher supply rate of the buoyant fluid can accelerate the ascent of the buoyant sheet.
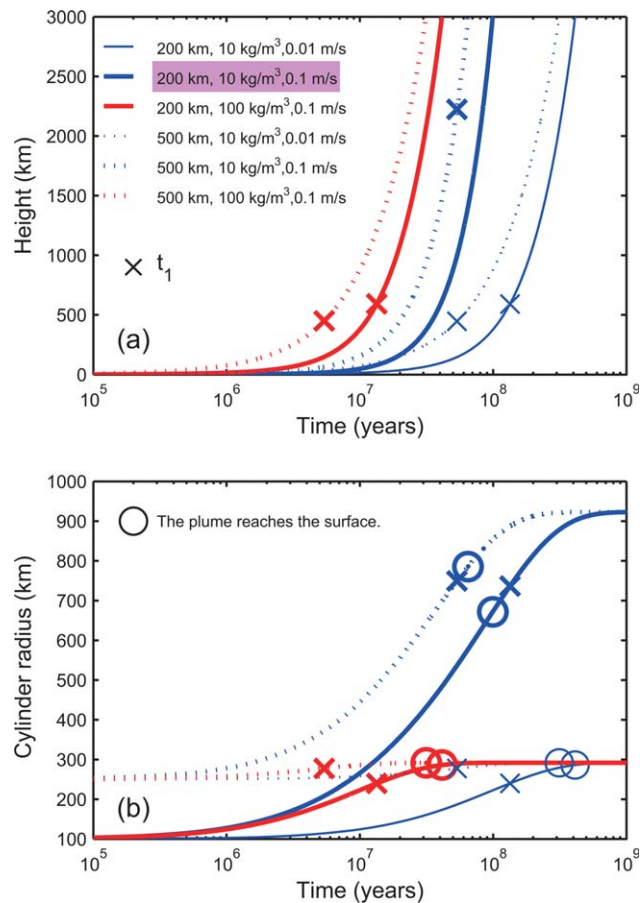

Figure 6. (a) Height evolution of buoyant sheet estimated by integrating equation (2) with equation (3). The adopted conditions are listed in the legends, which are the width of the sheet, w, the density difference between the inside and outside of the sheet, $\Delta\rho$, and the areal supply rate of buoyant fluids q/w. The viscosity of the ambient mantle is assumed as 10^{22} Pa·s. Crosses indicate the timing of t_1. In the case denoted by a thick blue curve whose legend is highlighted, the sheet can reach the surface before the gravitational instability separates the buoyant cylinder into spherical plume heads. (b) Corresponding radius of the buoyant cylinder for cases shown in Figure 6a. Circles show the time when the plume reaches the surface.

[50] These characteristics are confirmed by Figures 7a and 7b which shows the maximum heights that buoyant sheets can reach before the time scale for instability t_1 elapses. Figure 7a shows that buoyant sheets with smaller density differences and higher supply rates of buoyant fluid can ascend higher before gravitational instability changes its shape. The curve labeled as 3000 km shows the conditions under which the buoyant sheet can reach the surface of the Earth before gravitational instability occurs. Hence, when the buoyant sheet has conditions plotted in the upper left region of this curve, the sheet can reach the Earth's surface while maintaining its shape, as denoted by the inset cartoon. On the other hand, Figure 7b shows that thinner buoyant sheets can ascend higher before gravitational instability changes their shapes. These features are summarized in Figure 7c. Figure 7c is plotted by substituting $t = t_1$ and $h = 3000$ km in equation (11). The figure shows the conditions under which instabilities occur around the surface of the Earth. Again, within a reasonable supply rate of the buoyant fluid $q/w < 0.1$ m yr^{-1}, a thinner buoyant sheet with a smaller density difference can reach the surface of the Earth before instability occurs. This threshold becomes larger as the supply rate increases.

[51] We thus conclude that a thinner sheet with a smaller density difference from the surrounding mantle and a higher supply rate of buoyant fluid can reach the surface of the Earth while maintaining its sheet-like shape. If such a sheet with a buoyant cylinder reaches the surface, it could form an elongated LIP similar to the Ferrar LIP [*Elliot et al.*, 1999].

[52] The small density difference from the ambient mantle suggests that such a plume includes chemically heavy components and affects the composition of LIPs. This hypothesis is consistent with petrological observations [*Coffin and Eldholm*, 1994; *Ernst et al.*, 2005]. The anomalous composition in LIPs has also been suggested by seismic observations [*Korenaga*, 2011]. The estimated radius of the buoyant cylinder at the top of the sheet is approximately 600 km, as shown in Figure 6b. Although it has been recognized that a large plume head is required to generate LIPs [*Coffin and Eldholm*, 1994], 600 km as a cylinder radius is quite large. This discrepancy may originate from mechanisms that are not included in our experiments, such as background mantle convection and thermal diffusion. We will discuss the effect of thermal diffusion later.

[53] On the other hand, it is difficult for a wider buoyant sheet with a larger density difference and a lower supply rate of buoyant fluid to ascend while maintaining its shape without gravitational instability. Such a sheet must make several plume
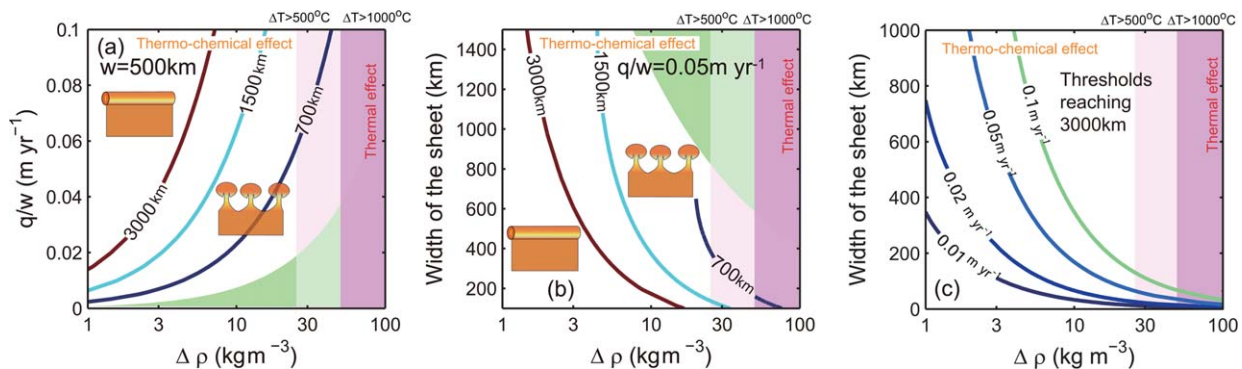

Figure 7. (a) Maximum heights that a buoyant sheet having a width of $w = 500$ km can reach before instability occurs as a function of density difference, $\Delta\rho$, and areal fluid supply rate, q/w, estimated from equations (9) and (11). The green region does not satisfy equation (5), as discussed in Figure 5, where our experimental results are not applicable. (b) Same as Figure 7a but as a function of the width of the buoyant sheet, and the areal supply rate of the buoyant fluid is $q/w = 0.05$ m yr^{-1}. The blue line is denoted only for the condition in which the width of the sheet is less than its height. (c) The conditions under which instability occurs at the surface of the Earth (3000 km). Contours indicate the areal fluid supply rate as a function of the density difference and the width of buoyant sheet. In Figures 7a–7c, the viscosity of the ambient mantle is assumed as 10^{22} Pa·s. The conditions assumed for the pink region are the same for Figure 5.

heads and may be observed as individual LIPs that are aligned. It is known that some LIPs erupt at similar ages [*Storey*, 1995], but there are not enough LIPs to allow us to discuss their linearity.

[54] The observed width of the SLVRP is about 500 km. The thick blue dotted curve in Figure 6 indicates that the time scale for the instability t_1 is shorter than the time scale for the buoyant sheet to reach the surface of the Earth, and that the difference between the two time scales is quite small. We here note that the time scale used to estimate the timing of instability, t_1, represents the time at which the top of the buoyant sheet undulates. At this stage, individual plume heads have not yet formed. In addition, thermal diffusion increases the time scale for instability in the mantle, as we will discuss later [*Kerr et al.*, 2008]. We thus infer that the SLVRP might erupt into an elongated LIP.

[55] The LLSVP beneath Africa is wider than 1200 km [*Ni and Helmberger*, 2003]. Such a wide ridge-like structure may have difficulty reaching the surface while maintaining its shape.

[56] In our experiments, we use a compositionally buoyant fluid, whereas in the Earth's mantle the buoyancy of the sheet-like upwelling originates from a hot thermal anomaly. If the sheet cools by thermal diffusion before it reaches the Earth's surface, its ascent may stop. The cooling time of the sheet by thermal diffusion is estimated using thermal diffusivity $\kappa = 10^{-6} \mathrm{m^2 s^{-1}}$, $t = (w/2)^2/\kappa$. In Figure 6, we assume the sheets are ≥ 200 km wide. For a width of 200 km, the cooling time becomes approximately $\sim 3 \times 10^8$ years. The time scale for the buoyant sheet to reach the surface is 10^8 years. We thus infer that the sheet discussed in Figure 6 can reach the surface before losing its buoyancy by thermal diffusion.

[57] Thermal diffusion also may affect the time scale of instability [*Kerr et al.*, 2008]. If thermal diffusion occurs before instability begins, thermal buoyancy decreases and gravitational instability is suppressed. For an isolated buoyant cylinder with a radius a, when the ratio of time scales for thermal diffusion and gravitational instability, equation (6), is smaller than $\Delta\rho g a^3/\kappa\mu_a < 300$, thermal diffusion delays the gravitational instability [*Kerr et al.*, 2008]. Figure 8 shows the calculated ratio $\Delta\rho g(w/2)^3/\kappa\mu_a$ for buoyant sheets. The ratio becomes smaller for a thinner sheet having smaller density differences. Although it is not obvious whether the threshold of 300 obtained for an isolated cylinder [*Kerr et al.*, 2008] is also ap-
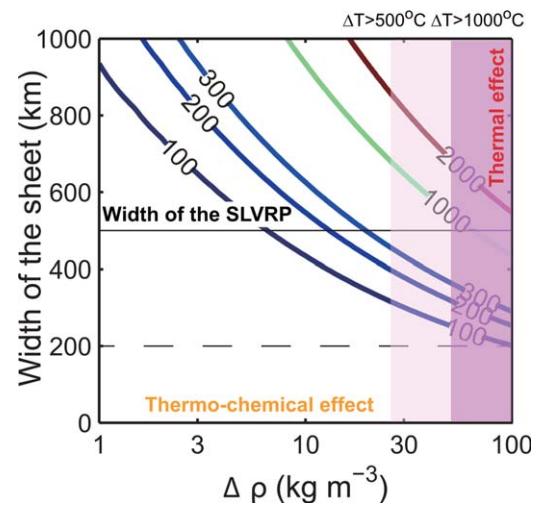

Figure 8. The contours show time scale ratios of thermal diffusion and instability, $\Delta\rho g(w/2)^3/\kappa\mu_a$, as a function of the density difference, $\Delta\rho$, and the width of the buoyant sheet w, [*Kerr et al.*, 2008]. The conditions assumed for the pink region are the same as those for Figure 5.

plicable to a sheet, the time scale for instability must be delayed for thinner sheets having smaller density differences. This is the same trend we find in Figure 7; that is, a sheet-like upwelling likely has a small density difference from the ambient mantle.

6. Conclusion

[58] We performed a series of experiments to estimate the parameter space in which the potentially buoyant SLVRP could reach the Earth's surface with maintaining its sheet-like structure. The buoyant fluid ascending from a line source accumulates at the top of the sheet in the shape of a cylinder. The cylinder eventually separates into spherical plume heads by gravitational instability. We formulate the time evolution of the buoyant sheet and the time scale until instability begins based on our experiments. Applying our model to the SLVRP, we find that a thinner and slightly buoyant sheet with sufficient supply of a buoyant fluid can reach the Earth's surface while maintaining its shape.

Appendix A: Prefactors in the Growth Time

[59] Figure A1a plots the calculated nondimensional growth rate as a function of wave number k using the long-wave asymptotic model written as equation (3.11) in *Lister et al.* [2011] with a variable viscosity ratio
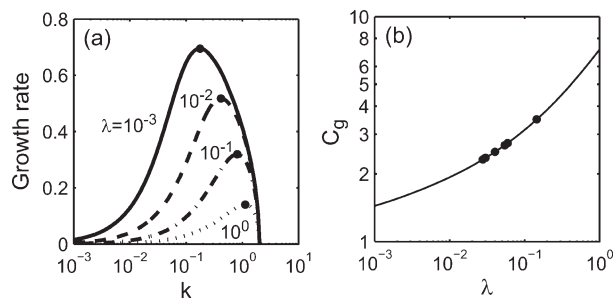
Figure A1. (a) Dispersion relation formulated in *Lister et al.* [2011] for various viscosity ratios λ. Black dots indicate the wave number at which growth rates become maximal. The growth rate is normalized by $\Delta\rho g a/\mu_a$. (b) Calculated C_g in equation (6) for the most unstable growth time, which is an inverse of the growth rate in Figure A1a. Black dots indicate the values used in our experiments.

$\lambda = \mu_i/\mu_a$. Figure A1b is the prefactor of the growth time C_g in equation (6) to maximize the growth rate in Figure A1a.

Acknowledgments

References

Bercovici, D., and A. Kelly (1997), The non-linear initiation of diapirs and plume heads, *Phys. Earth Planet. Inter.*, *101*, 119–130.

Bercovici, D., G. Schubert, G. A. Glatzmaier, and A. Zebib (1989), Three-dimensional thermal convection in a spherical shell, *J. Fluid Mech.*, *206*, 75–104.

Bryan, S. E., and R. E. Ernst (2008), Revised definition of Large Igneous Provinces (LIPs), *Earth Sci. Rev.*, *86*, 175–202.

Coffin, M. F., and O. Eldholm (1994), Large igneous provinces: Crustal structure, dimensions, and external consequences, *Rev. Geophys.*, *32*, 1–36.

Cordery, M. J., G. F. Davies, and I. H. Campbell (1997), Genesis of flood basalts from eclogite-bearing mantle plumes, *J.Geophys. Res.*, *102*, 20,179–20,197.

Davaille, A. (1999), Simultaneous generation of hotspots and superswells by convection in a heterogeneous planetary mantle, *Nature*, *402*, 756–760.

Deschamps, F., E. Kaminski, and P. J. Tackley (2011), A deep mantle origin for the primitive signature of ocean island basalt, *Nat. Geosci.*, *4*, 879–882.

Elliot, D. H., T. H. Fleming, P. R. Kyle, and K. A. Foland (1999), Long-distance transport of magmas in the Jurassic Ferrar Large Igneous Province, Antarctica, *Earth Planet. Sci. Lett.*, *167*, 89–104.

Ernst, R. E., K. L. Buchan, and I. H. Campbell (2005), Frontiers in large Igneous Province research, *Lithos*, *79*, 271–297.

Farnetani, C. G., and H. Samuel (2005), Beyond the thermal plume paradigm, *Geophys. Res. Lett.*, *32*, L07311, doi:10.1029/2005GL022360.

Garnero, E. J., and A. K. McNamara (2008), Structure and dynamics of Earth's lower mantle, *Science*, *320*, 626–628.

Gonnermann, H. M., M. Manga, and A. M. Jellinek (2002), Dynamics and longevity of an initially stratified mantle, *Geophys. Res. Lett.*, *29*(10), 1399, doi:10.1029/2002GL014851.

Griffiths, R. W., and I. H. Campbell (1990), Stirring and structure in mantle starting plumes, *Earth Planet. Sci. Lett.*, *99*, 66–78.

He, Y., and L. Wen (2009), Structural features and shear-velocity structure of the "Pacific Anomaly", *J. Geophys. Res.*, *114*, B02309, doi:10.1029/2008JB005814.

Jaupart, C., P. Molnar, and E. Cottrell (2007), Instability of a chemically dense layer heated from below and overlain by a deep less viscous fluid, *J. Fluid Mech.*, *572*, 433–469.

Kerr, R. C., and J. R. Lister (1988), Island arc and mid-ocean ridge volcanism, modelled by diapirism from linear source regions, *Earth Planet. Sci. Lett.*, *88*, 143–152.

Kerr, R. C., C. Mériaux, and J. R. Lister (2008), Effect of thermal diffusion on the stability of strongly tilted mantle plume tails, *J. Geophys. Res.*, *113*, B09401, doi:10.1029/2007JB005510.

Korenaga, J. (2011), Velocity-depth ambiguity and the seismic structure of large igneous provinces: A case study from the Ontong Java plateau, *Geophys. J. Int.*, *185*, 1022–1036.

Kumagai, I., A. Davaille, K. Kurita, and E. Stutzmann (2008), Mantle plumes: Thin, fat, successful, or failing?, Constraints to explain hot spot volcanism through time and space, *Geophys. Res. Lett.*, *35*, L16301, doi:10.1029/2008GL035079.

Lin, S., and P. E. van Keken (2006), Dynamics of thermochemical plumes: 2. Complexity of plume structures and its implications for mapping mantle plumes, *Geochem. Geophys. Geosyst.*, *7*, Q03003, doi:10.1029/2005GC001072.

Lister, J. R., and R. C. Kerr (1989), The effect of geometry on the gravitational instability of a buoyant region of viscous fluid, *J. Fluid Mech.*, *202*, 577–594.

Lister, J. R., R. C. Kerr, N. J. Russell, and A. Crosby (2011), Rayleigh-Taylor instability of an inclined buoyant viscous cylinder, *J. Fluid Mech.*, *671*, 313–338.

McNamara, A. K., and S. Zhong (2005), Thermochemical structures beneath Africa and the Pacific Ocean, *Nature*, *437*, 1136–1139.

Mitrovica, J. X., and A. M. Forte (2004), A new inference of mantle viscosity based upon joint inversion of convection and glacial isostatic adjustment data, *Earth Planet. Sci. Lett.*, *225*, 177–189.

Nakagawa, T., P. J. Tackley, F. Deschamps, and J. A. D. Connolly (2009), Incorporating self-consistently calculated mineral physics into thermochemical mantle convection simulations in a 3-D spherical shell and its influence on seismic anomalies in Earth's mantle, *Geochem. Geophys. Geosyst.*, *10*, Q03004, doi:10.1029/2008GC002280.

Namiki, A. (2003), Can the mantle entrain D″?, *J. Geophys. Res.*, *108*(B10), B102487, doi:10.1029/2002JB002315.

Ni, S., and D. V. Helmberger (2003), Seismological constraints on the South African superplume; could be the oldest distinct structure on earth, *Earth Planet. Sci. Lett.*, *206*, 119–131.

Ni, S., E. Tan, M. Gurnis, and D. Helmberger (2002), Sharp sides to the African superplume, *Science*, *296*, 1850–1852.

Oganov, A. R., J. P. Brodholt, and G. D. Price (2001), The elastic constants of MgSiO$_3$ perovskite at pressures and temperatures of the Earth's mantle, *Nature*, *411*, 934–937.

Olson, P., and C. Kincaid (1991), Experiments on the interaction of thermal convection and compositional layering at the base of the mantle, *J. Geophys. Res.*, *96*, 4347–4354.

Olson, P., and H. Singer (1985), Creeping plumes, *J. Fluid Mech.*, *158*, 511–531.

Steinberger, B., and T. H. Torsvik (2012), A geodynamic model of plumes from the margins of Large Low Shear Velocity Provinces, *Geochem. Geophys. Geosyst.*, *13*, Q01W09, doi:10.1029/2011GC003808.

Storey, B. C. (1995), The role of mantle plume in continental breakup: Case histories from Gondwanaland, *Nature*, *377*, 301–308.

Sun, D., D. Helmberger, and M. Gurnis (2010), A narrow, mid-mantle plume below southern Africa, *Geophys. Res. Lett.*, *37*, L09302, doi:10.1029/2009GL042339.

Tackley, P. J. (2012), Dynamics and evolution of the deep mantle resulting from thermal, chemical, phase and melting effects, *Earth Sci. Rev.*, *110*, 1–25.

Takeuchi, N. (2012), Detection of ridge-like structures in the Pacific Large-Shear-Velocity Province, *Earth Planet. Sci. Lett.*, *319-320*, 55–64.

Tan, E., and M. Gurnis (2007), Compressible thermochemical convection and application to lower mantle structures, *J. Geophys. Res.*, *112*, B06304, doi:10.1029/2006JB004505.

Tan, E., W. Leng, S. Zhong, and M. Gurnis (2011), On the location of plumes and lateral movement of thermochemical structures with high bulk modulus in the 3-D compressible mantle, *Geochem. Geophys. Geosyst.*, *12*, Q07005, doi:10.1029/2011GC003665.

Taylor, B. (2006), The single largest oceanic plateau: Ontong Java-Manihiki-Hikurangi, *Earth Planet. Sci. Lett.*, *241*, 372–380.

To, A., B. Romanowicz, Y. Capdeville, and N. Takeuchi (2005), 3D effects of sharp boundaries at the borders of the African and Pacific superplumes: Observation and modeling, *Earth Planet. Sci. Lett.*, *233*, 137–153.

Torsvik, T. H., M. A. Smethurst, K. Burke, and B. Steinberger (2006), Large igneous provinces generated from the margins of the large low-velocity provinces in the deep mantle, *Geophys. J. Int.*, *167*, 1447–1460.

van Heck, H. J., and P. J. Tackley (2008), Planforms of self-consistently generated plates in 3D spherical geometry, *Geophys. Res. Lett.*, *35*, L19312, doi:10.1029/2008GL035190.

van Keken, P. E., E. H. Hauri, and C. J. Ballentine (2002), Mantle mixing: The generation, preservation, and destruction of chemical heterogeneity, *Annu. Rev. Earth Planet. Sci.*, *30*, 493–525.

Wang, Y., and L. Wen (2007), Geometry and P and S velocity structure of the "African Anomaly", *J. Geophys. Res.*, *112*, B05313, doi:10.1029/2006JB004483.

Whitehead, J. A., and D. S. Luther (1975), Dynamics of laboratory diapir and plume models, *J. Geophys. Res.*, *80*, 705–717.